Optical Materials: X 16 (2022) 100206

Contents lists available at ScienceDirect

Optical Materials: X

journal homepage: www.journals.elsevier.com/optical-materials-x

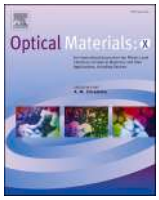

Highly red luminescent stabilized tetragonal rare earth-doped HfO_2 crystalline ceramics prepared by sol-gel

Fernanda Hediger Borges [a], Douglas Silva da Hora Oliveira [a], Giulia Paulino Hernandes [a], Sidney José Lima Ribeiro [b], Rogéria Rocha Gonçalves [a,*]

[a] Laboratório de Materiais Luminescentes Micro e Nanoestruturados –Mater Lumen, Departamento de Química, FFCLRP, Universidade de São Paulo, SP, Brazil
[b] Instituto de Química, São Paulo State University, Araraquara, SP, Brazil

A B S T R A C T

We report high incorporation of rare earth ions (RE^{3+}) into hafnia nanoparticles prepared by the sol–gel method and investigate how these dopants affect hafnia structure and phase transformation. An ethanolic suspension containing 5-nm hafnia nanoparticles was obtained from $HfOCl_2.8H_2O$ in ethanol. Pure and 0.1–7 mol% Eu^{3+}-doped materials afforded HfO_2 monoclinic phase, whereas hafnia nanoparticles added with 10 and 20 mol% Eu^{3+} were stabilized in the tetragonal phase. Structural evolution of the nanoparticles was analyzed by Eu^{3+} luminescence spectroscopy and excited level lifetimes. The emission spectra in the visible region showed an increase of the Eu^{3+} site symmetry due to hafnia phase transformation from monoclinic to tetragonal upon increasing Eu^{3+} concentration. Concentration quenching, followed by lifetime measurements, occurred at high Eu^{3+} concentration (20 mol %). The hafnia tetragonal phase was stabilized with non-optically active La^{3+} (a fixed concentration of 10 mol %), co-doped with a lower concentration of Eu^{3+} ions (from 0.1 to 3 mol %). This strategy ensured that Eu^{3+} luminescence in tetragonal hafnia was intense and prevented quenching by the high Eu^{3+} concentration. In this sense, the hafnia structure and emission properties can be tailored by the RE^{3+} concentration, so that an interesting material for applications in photonics and biophotonics can be achieved.

1. Introduction

Due to its interesting physical and chemical properties, hafnium dioxide (HfO_2) is a promising and versatile material with potential application in engineered ceramics, electronic materials, optoelectronics, and solid electrolytes, to name a few. High chemical and thermal stability, high mechanical resistance, high melting point (2800 °C), and high phase transition temperatures are desirable properties in high-temperature refractory materials acting as ultra-high temperature ceramics for use in the thermal oxidation of protection layer systems and thermal barrier coatings [1–7]. In addition, HfO_2 has high neutron cross-section absorption coefficient, which is useful in the nuclear industry [8]. The high HfO_2 dielectric constant ($\varepsilon = 16$–70, depending on the crystalline phase) [9] makes it an excellent candidate to substitute SiO_2 in high-k gate dielectrics in complementary metal-oxide semiconductors (CMOS) [10]. Over the last decade, interest in this particular host has grown mostly because of its ferroelectric properties, not to mention that these systems are suitable for memory applications, ferroelectric random-access memory (FeRAM), and ferroelectric field-effect transistor (FeFET) [11–13].

Besides these properties, HfO_2 has characteristics that allow it to be employed as optical material. It has high refractive index (n~2.1 at 550 nm) [14,15] and wide band gap (5.3–5.9 eV) [16], transparency in the near-UV (below 300 nm) and IR (10 μm) regions [14], and low phonon energy (<700 cm^{-1}) [17]. Furthermore, HfO_2 is a suitable host for lanthanide ions, and high concentrations of these ions can be incorporated into this host [18]. For optical applications, HfO_2 can be used in combination with SiO_2 layers, to form high index contrast multilayer structures with high laser damage thresholds; this material can also be employed as anti-reflex coating [19,20]. Moreover, HfO_2-based materials are excellent candidates for optical amplification and planar waveguides. In fact, Er^{3+}-doped SiO_2-HfO_2 is one of the best systems for 1.5-μm applications in the telecommunication field—it is an effective waveguide with broad bandwidth (~50 nm), low attenuation coefficient (0.8 dB/cm at 1.5 μm), and efficient luminescence [18,21–25]. The high density of HfO_2 (9.68 g/cm^3) and its high atom number ($Z = 72$, $Z_{eff} = 67.2$) [26–29] make it an attractive host for heavy scintillators, aiming at applications in bioimaging, radioluminescence, and dosimetry [30–34]. Combined with its non-toxicity and inertness to living organisms, HfO_2-based systems could be applied for *in vivo* diagnosis and therapy [35–39].

Although ZrO_2-based materials have been widely studied, the analogous oxide HfO_2 has gained attention over the years. Hafnium and zirconium have almost identical properties and are known as the twins

* Corresponding author.
E-mail address: rrgoncalves@ffclrp.usp.br (R.R. Gonçalves).

https://doi.org/10.1016/j.omx.2022.100206
Received 9 August 2022; Received in revised form 13 October 2022; Accepted 19 October 2022
Available online 11 November 2022

of the periodic table. The atomic radii, and thus the ionic radii, of both elements are quite similar (Zr^{4+} = 0.84 Å, and Hf^{4+} = 0.83 Å, for coordination number (CN) = 8) [40] as a result of the so-called lanthanide contraction. Consequently, ZrO_2 and HfO_2 have analogous chemical properties. Like ZrO_2, HfO_2 has three polymorphs at normal pressure: monoclinic, tetragonal, and cubic. In a pure ZrO_2/HfO_2 ceramic, the monoclinic phase is stabilized at room temperature, while the tetragonal and the cubic phases only arise at very high temperature. HfO_2 phase transformation from the monoclinic to the tetragonal structure and from the latter structure to the cubic structure occurs at 1720 and 2600 °C, respectively, and the cubic phase is stable up to a melting point of 2800 °C [8]. HfO_2 has higher phase transformation temperatures than ZrO_2, so it is a strong candidate to replace ZrO_2-based materials, especially for applications in high-temperature ceramics [8]. Additionally, the technological importance of the tetragonal and cubic polymorphs is well-known (e.g., the higher k values of these phases), so stabilization of these phases at low temperature is desirable [41,42].

Addition of ions with lower valence than Hf^{4+}; i.e., divalent or trivalent ions, can fully (or partially) stabilize the HfO_2 tetragonal and cubic phases at low temperature, to form solid solutions. The stabilization mechanisms resemble the stabilization mechanisms of ZrO_2 [43–45]. Incorporation of dopants into HfO_2 creates defects and oxygen vacancies due to differences in charge and ionic radii between the dopants and Hf^{4+}. The more Hf^{4+} ions are substituted for heterovalent dopants, the higher the increase in the concentration of oxygen vacancies for charge compensation, thereby stabilizing the tetragonal and cubic phases [46,47]. These vacancies are randomly arranged in the local surroundings of Hf^{4+}, creating several slightly different sites with diverse coordination [48]. Given that the luminescent properties of lanthanide ions strongly depend on the crystalline structure of the host, these different arrangements directly reflect on their emission. Eu^{3+}, which has unique luminescent properties due to its specific levels and assigned electronic transitions, can be used as a structural probe and is an excellent tool to identify phase transformations. Analysis of the relative intensity of the Eu^{3+} $^5D_0 \rightarrow {}^7F_J$ (J = 0–6) transitions and of the number of Stark components of the $^7F_{0-4}$ levels allows the local structure of the host to be explored and the symmetry sites where Eu^{3+} is located to be studied [49].

Tailoring the desired HfO_2 phase by introducing rare earth dopants (RE^{3+}) depends on the concentration and ionic radius of these ions [46]. In general, RE^{3+} are highly soluble in these substitutional solid-solution RE_2O_3-HfO_2 systems. The monoclinic, tetragonal, and cubic fluorite-type phases are stabilized upon increasing RE^{3+} concentration (up to 80 mol% RE^{3+} [46]) without clusters being formed. Therefore, these systems have attracted attention as very efficient luminescent systems where concentration quenching processes are avoided [50]. In addition, more than one type of dopant can be incorporated, enabling phase formation and optical properties to be controlled, to boost the intensity of RE^{3+} luminescence [18,29,31,51].

In this sense, here we report a detailed study of RE^{3+}-doped HfO_2 colloidal suspensions and powders prepared by the sol–gel method. We describe the structural changes and stabilization of the crystalline phases of the different HfO_2 polymorphs as a function of the RE^{3+} concentration. We also investigate the luminescent properties of the systems by varying the Eu^{3+} concentration and following the structural changes in their emission spectra, with Eu^{3+} serving as structural probe. We show how we have tailored the structure of the HfO_2 host by stabilizing the tetragonal phase at low temperature after incorporation of non-luminescent La^{3+} at a fixed concentration of 10 mol% and varied Eu^{3+} concentration, in order to ensure that the desired structural phase is formed while preventing concentration quenching. In fact, this approach allowed us to achieve phase control with incorporation of high RE^{3+} concentration, proving that the dopants are highly soluble in the host, while luminescence quenching is negligible. By combining phase control and great luminescent features, we have been able to design an interesting system for optical applications in photonics and biophotonics.

2. Experimental procedure

2.1. Preparation of colloidal suspension

Hafnia nanoparticles were prepared from a suspension of $HfOCl_2$ in ethanol (0.4 M). The mixture was kept under reflux for 2 h. The optimized reflux conditions were 90 °C for 1 h, which gave a transparent solution of particles with diameter of 2–8 nm (measured by photon correlation spectroscopy (PCS) and high-resolution transmission electronic microscopy (HRTEM)). To obtain RE^{3+}-doped HfO_2, $LnCl_3$ (Ln = Eu or La) was added to the reflux, and the same treatment was applied. HfO_2 doped with 0.1–20 mol % Eu^{3+} and co-doped with 10 mol % La^{3+} and 0.1–3 mol% Eu^{3+} were obtained.

2.2. Preparation of powders

Eu^{3+}-doped and La^{3+}/Eu^{3+} co-doped HfO_2 powders were prepared by addition of NH_4OH to an ethanolic suspension of hafnium oxychloride, which immediately gave non-transparent gels. The resulting gels were isolated by centrifugation, washed with water several times, dried, and annealed at 700 or 900 °C for 2 h.

2.3. Characterization

To observe the average diameter, the particles of the colloidal suspension were measured by PCS (Brookhaven equipment with a laser of 543.5 nm) and HRTEM (HRTEM-CM200 FEG, Philips). The powders were characterized by X-ray diffraction (XRD) recorded on a diffractometer (D-5005 S) operating with a CuKα filtered line. The 2θ values ranged from 5 to 70°; the scanning rate was 0.02° s^{-1}.

The spectroscopic measurements were performed at room temperature on a Spectrofluorimeter HITACHI, F-3010. A 150-W Xe lamp was used as the excitation source, and a photomultiplier was employed as detector. A simple monochromator with 1.5-nm was used. Other measurements were accomplished on a Spectrofluorimeter SPEX, Fluorolog F212l, equipped with a 450-W Xe lamp, double monochromator model 1680, and a Hamamatsu R928 photomultiplier.

3. Results and discussion

We characterized the colloidal suspensions by PCS, to observe the presence of nanoparticles, and HRTEM, to determine the size, structure, and morphology of the colloids. Fig. 1b shows the typical size distribution of the system. The nanoparticles measure between 5 and 10 nm, irrespective of the Eu^{3+} concentration. Fig. 1a shows nanocrystals measuring 4–6 nm. The interplanar distance, 3.17 Å (hkl 111 for monoclinic HfO_2 (JCPDS 34-104)), suggests the presence of HfO_2 in the monoclinic structure. An amorphous phase also emerges along with the crystalline particles, but aggregates are absent. Fig. 1b represents the narrow size distribution of HfO_2 nanoparticles doped with 1 mol% Eu^{3+}, and Table 1 lists the mean size measured by PCS with increasing Eu^{3+} concentration in the HfO_2 host.

XRD was employed to analyze the structure of the powders obtained through hydrolysis followed by annealing at 700 °C. Fig. 2 shows the diffractograms of pure and Eu^{3+}-doped HfO_2:Eu^{3+} concentrations range from 0.1 to 20 mol%.

The HfO_2 monoclinic phase, space group $P2_1/c$ (ICSD collection code 27313, JCPDS 34-104) was identified for pure HfO_2 and HfO_2 added with a small quantity of Eu^{3+} (0.1 or 1.0 mol %). The unit cell dimensions are a = 5.117, b = 5.175, and c = 5.292 Å; β = 99.216° [53]. In this structure, Hf^{4+} is coordinated with seven oxygen atoms; the oxygen atoms are non-equivalent and alternate between three- and fourfold coordination. The fourfold oxygens form the base of a cube, with average Hf–O distances of 2.197 Å. The threefold oxygens are arranged

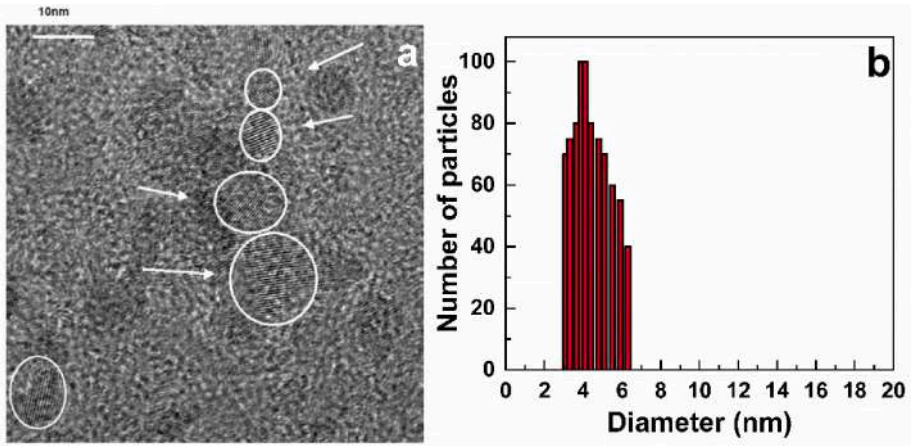

Fig. 1. a) HRTEM micrography of the colloidal suspension of Eu^{3+}-doped HfO_2 and b) size distribution of HfO_2 nanoparticles doped with 1 mol% Eu^{3+}.

Table 1
Mean size of pure and Eu^{3+}-doped HfO_2 nanoparticles in colloidal suspension observed by PCS measurements.

Eu^{3+} concentration (mol %)	Mean size (nm)
-	6.3
1	5.5
5	8.0
7	7.8
10	4.7
20	9.0

as one oxygen atom at the upper corner and two oxygen atoms in the middle of the edges of the cube; however, the average Hf–O bond distance is shorter: 2.086 Å [54]. The primitive cell contains four HfO_2 formula units [55].

Addition of 10–20 mol% Eu^{3+} affords a stabilized HfO_2 tetragonal phase, space group $P4_2/nmc$ (ICSD collection code 173966), with unit cell parameters a = 3.577 and c = 5.200 Å. The HfO_2 tetragonal phase resembles the ZrO_2 tetragonal phase [8], so an analogy can be made. The tetragonal phase is a distortion of the ideal fluorite-cubic structure [56]. In this structure, Zr^{4+} is coordinated with eight oxygen atoms. Four oxygen atoms are in an elongated tetrahedron, whereas the other four oxygen atoms are in a flattened tetrahedron; the Zr–O distances are 2.455 and 2.065 Å, respectively. The second tetrahedron is rotated by 90° in relation to the first tetrahedron [56]. In sum, a tetragonal solid solution arises for HfO_2 with higher Eu^{3+} concentration (>10 mol%), while 5 and 7 mol% Eu^{3+}-doped HfO_2 contain a mixture of the monoclinic and tetragonal phases. A previous work described a similar structural behavior for 0.1, 1, and 10 mol% Er^{3+}-doped HfO_2 [18].

As mentioned previously, the tetragonal and cubic structures can be

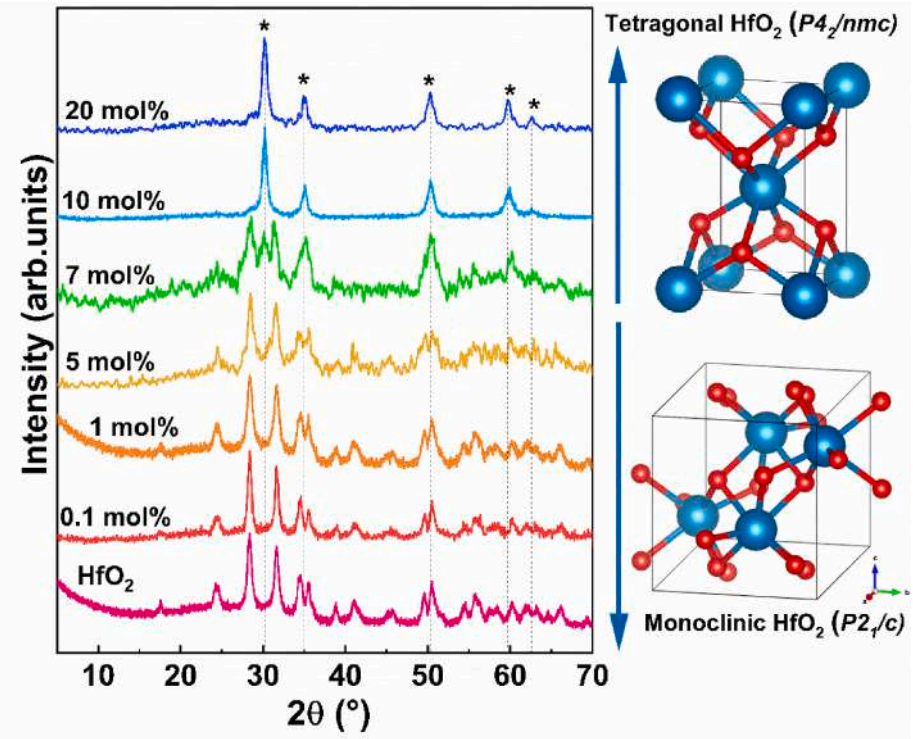

Fig. 2. X-ray diffractograms of pure HfO_2 and 0.1–20 mol% Eu^{3+}-doped HfO_2 annealed at 700 °C. The tetragonal phase planes are identified with (*). Standard visualization of the tetragonal and monoclinic HfO_2 crystalline phases. The blue and red colors refer to the Hf and O atoms, respectively. The unit cells were designed with the VESTA software [52]. (For interpretation of the references to color in this figure legend, the reader is referred to the Web version of this article.)

achieved at very low temperature by doping HfO_2 and ZrO_2 with RE^{3+}, resulting in a solid solution. The oxygen vacancies, formed by charge compensation when two Hf^{4+} or Zr^{4+} ions are replaced with two RE^{3+} ions, are randomly distributed in an anionic sub-lattice. The RE^{3+} ions occupy the Hf^{4+} or Zr^{4+} sites in the lattice, tending to coordinate with eight oxygen atoms, which is the coordination number (CN) of the tetravalent ions in both the tetragonal and cubic structures. This creates oxygen vacancies around Hf^{4+} or Zr^{4+}. The strong covalent nature of the Hf–O or Zr–O bond favors the sevenfold coordination, as in the case of the monoclinic structure. In this sense, the average coordination number of Hf^{4+} or Zr^{4+} is effectively lower upon doping, to stabilize the tetragonal and cubic phases at lower temperatures [44,47,57]. Therefore, the monoclinic, tetragonal, or cubic structure can be achieved depending on the concentration of the different RE^{3+}; i.e., the structure can be tailored by the molar amount and size of the dopant(s) [46,58].

In the literature, attribution of the tetragonal and cubic crystalline phases is commonly misinterpreted when only conventional XRD analysis is performed. The XRD patterns of both phases are almost identical. The only difference is the peak with $2\theta > 60°$, so the phases can be better distinguished by high-resolution synchrotron X-ray powder diffraction [1]. In a previous paper, our group used FTIR spectroscopy to demonstrate a simple and conclusive method to identify the three different HfO_2 polymorphs (monoclinic, tetragonal, and cubic). On the basis of group theory, six vibrational modes are IR-active for the tetragonal phase ($2A_{2u}+4E_u$) [1,59,60], whereas only one active mode is expected for the cubic phase (F_{1u}). In the FTIR spectra of HfO_2 doped with different Er^{3+} concentrations, films deposited on a Si substrate, annealed at 900 °C, present at least five IR modes, which definitely indicate stabilization of the tetragonal phase, and not of the cubic phase [18]. Thus, we assumed that Eu^{3+}-doped HfO_2 containing lower and higher Eu^{3+} concentration are in the monoclinic and tetragonal crystalline phase, respectively, in accordance to Cunha et al. [18].

The Eu^{3+} emission spectra allowed us to explore the local structure where RE^{3+} is located in the different stabilized HfO_2 structures. Fig. 3 shows the emission spectra of 0.1–10 mol% Eu^{3+}-doped HfO_2 powder annealed at 700 °C under excitation at 394 nm, corresponding to the Eu^{3+} $^7F_0 \rightarrow {}^5L_6$ transition. The Eu^{3+} 4f intraconfigurational transitions have been assigned to emission from the $^5D_0$ excited level to the ^7F_J fundamental level, where J = 0, 1, 2, 3, and 4. The number of the Stark components and the relative intensity of the transitions change with the structural transformations and variations in the positions of the neighboring atoms.

HfO_2 with lower Eu^{3+} concentration (0.1 or 1 mol%), where the monoclinic phase is stabilized, displays spectra typical of Eu^{3+} in the monoclinic phase, agreeing with the literature [61–63]. On the other hand, HfO_2 with higher Eu^{3+} concentration (10 mol%), where the tetragonal phase is stabilized, exhibits broader and completely different spectra, showing that Eu^{3+} occupies different symmetry sites. Emission of the $^5D_0 \rightarrow {}^7F_2$ transition centered at ~606 nm is associated with Eu^{3+} in tetragonal HfO_2 or ZrO_2 [43]. HfO_2 with 5 or 7 mol% Eu^{3+} presents an intermediate profile, and we detected a structural transformation. The spectra still resemble the spectrum of Eu^{3+} in the monoclinic phase, but the bands characteristic of Eu^{3+} are broader, indicating the presence of some material in the tetragonal phase. The emission spectra clearly show the structural changes observed in the XRD analysis. Later, we will discuss these crystalline structures.

Two different spectra were recorded, representative of each system: monoclinic structure, for the sample doped with 1 mol% Eu^{3+}, and tetragonal solid solution, for the sample doped with 10 mol% Eu^{3+}. These spectra are depicted in Fig. 4.

Compared to the bands typical of Eu^{3+} crystals, the bands herein are generally broader due to mismatch between the ionic radii and charges of Hf^{4+} and Eu^{3+} ($rEu^{3+} = 1.01$ and $rHf^{4+} = 0.76$ Å, for CN = 7) [40], which distort the lattice and promote oxygen vacancies. For both stabilized HfO_2 and ZrO_2, the oxygen vacancies may shift the positions of the atoms as compared to the fluorite structure, leading to local site deformation. The presence of these vacancies defines a large quantity of different symmetry sites with coordination number 6, 7, and 8, and the contribution of this group of sites is responsible for broadening of the emission bands. This can originate various slightly different symmetry sites, giving rise to this inhomogeneous enlargement of the linewidths [18,48,62]. This behavior can be classified as intermediate between the behavior observed in perfect crystals and the one observed in glasses [64].

For the two HfO_2 polymorphs observed in this work, the overall symmetry increases on going from the monoclinic to the tetragonal phase, where the lattice has symmetry C_{2h} and D_{4h}, respectively [65,66].

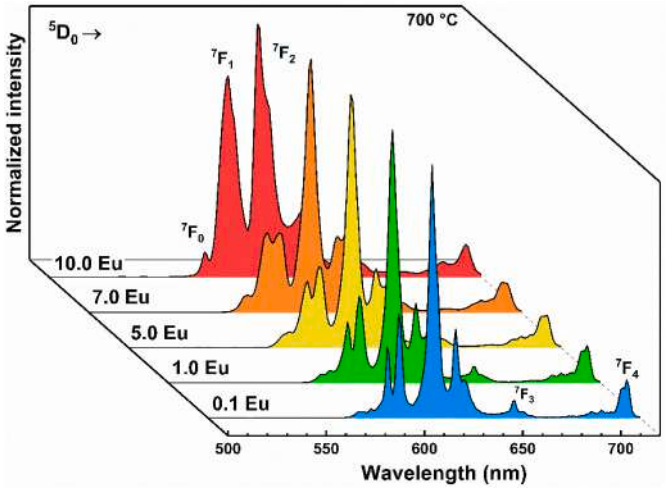

Fig. 3. Emission spectra under excitation at 394 nm of Eu^{3+}-doped HfO_2 annealed at 700 °C.

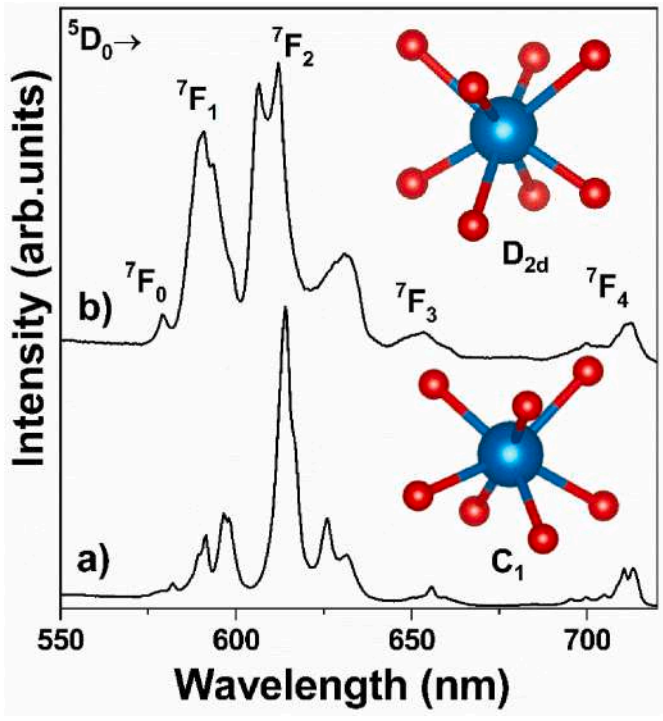

Fig. 4. Emission spectra of the Eu^{3+}-doped HfO_2 powders annealed at 700 °C, with Eu^{3+} concentrations of: a) 1 mol% and b) 10 mol%. The inset shows the symmetry sites of the Hf atoms in both structures (the figures were made from the unit cells of the monoclinic and tetragonal phases; the VESTA software was used [52]).

Therefore, Eu^{3+} is expected to occupy higher symmetry sites upon increasing Eu^{3+} concentration, as a result of phase transformation. This difference in symmetry can be clearly noted by the relative intensity of the $^5D_0 \rightarrow {}^7F_2$ and $^5D_0 \rightarrow {}^7F_1$ transitions. The $^5D_0 \rightarrow {}^7F_1$ is a magnetic dipole transition, allowed by the Laporte selection rule; it does not depend on the chemical environment and is used as a reference for comparison to the intensity of other transitions. The $^5D_0 \rightarrow {}^7F_2$ transition is known as a hypersensitive transition and strongly depends on the environment in which Eu^{3+} is inserted [49]. By calculating the ratio between the $^5D_0 \rightarrow {}^7F_2/{}^5D_0 \rightarrow {}^7F_1$ intensities (also known as asymmetric ratio) [67], we obtain strong indication of the Eu^{3+} local environment. A lower value for this ratio suggests a site with higher symmetry. Here, we calculated these ratios on the basis of the respective emission spectrum, fitted by Lorentzian functions, and we took the areas of each corresponding Eu^{3+} transition into consideration. The values are displayed in Table 2. We found values of about 3.1 for monoclinic Eu^{3+}-doped HfO_2 (0.1–5.0 mol % Eu^{3+}). This value decreased with increasing Eu^{3+} concentration. For 7 mol% Eu^{3+}-doped HfO_2, the value is intermediate, whilst 10 mol% Eu^{3+}-doped HfO_2, a tetragonal sample, has a value of 1.9. Therefore, the Eu^{3+} surroundings change from lower to higher symmetry in the monoclinic and tetragonal phases, respectively.

For the ZrO_2 monoclinic crystalline structure, sevenfold coordinated Zr^{4+} is in symmetry C_1 [65,68]. Similarly, in HfO_2, Eu^{3+} enters this low symmetry site C_2/C_1 [43]. The low Eu^{3+} symmetry in this structure is revealed by the dominant $^5D_0 \rightarrow {}^7F_2$ transition, indicating that Eu^{3+} is in a non-centrosymmetric site. Also, the $^5D_0 \rightarrow {}^7F_0$ transition is only observed in symmetries C_{nv}, C_n, and C_s [49], confirming that the local Eu^{3+} environment is asymmetric in monoclinic HfO_2.

On the other hand, we expected higher symmetry for Eu^{3+} in the tetragonal phase. The symmetry of eightfold coordinated Zr^{4+} is D_{2d} in the tetragonal structure [48,65,68]. For this symmetry, 0, 2, and 2 bands are expected for the $^5D_0 \rightarrow {}^7F_{0,1,2}$ transitions, respectively. However, we observed something different in the spectra recorded herein. Some authors [48,65,68] have stated that the tetrahedra surrounding oxygen are expanded in the *c* direction, which can lead to site symmetry C_{2v} [65]. Additionally, replacement with larger ions reduces the symmetry. Likewise, Eu^{3+} should replace Hf^{4+} in a site with symmetry D_{2d} in tetragonal HfO_2 [43], but we also observed reduced symmetry in Fig. 3b. Despite the higher symmetry in the tetragonal structure as compared to the monoclinic structure, the $^5D_0 \rightarrow {}^7F_2$ transition clearly stands out over the $^5D_0 \rightarrow {}^7F_1$ transition, evidencing lack of an inversion center. Furthermore, the $^5D_0 \rightarrow {}^7F_0$ transition, which is forbidden in symmetry D_{2d} [49], is evident, once again attesting to lower symmetry and more disordered structure in the present case.

Table 2
$^5D_0 \rightarrow {}^7F_2/{}^5D_0 \rightarrow {}^7F_1$ intensity ratios (asymmetric ratio) and CIE 1931 chromaticity color coordinates for Eu^{3+}-doped and La^{3+}/Eu^{3+} co-doped HfO_2 annealed at 700 and 900 °C upon excitation at 394 nm.

Annealing temperature (°C)	Eu^{3+} concentration (mol %)	La^{3+} concentration (mol %)	$\frac{^5D_0 \rightarrow {}^7F_2}{^5D_0 \rightarrow {}^7F_1}$	Color coordinates (*x*, *y*)
700	0.1	–	3.1	(0.651, 0.348)
	1.0	–	3.3	(0.652, 0.348)
	5.0	–	3.1	(0.649, 0.350)
	7.0	–	2.8	(0.646, 0.353)
	10.0	–	1.9	(0.631, 0.368)
900	0.1	–	3.4	(0.651, 0.348)
	1.0	–	3.3	(0.652, 0.347)
	10.0	–	2.0	(0.633, 0.367)
	20.0	–	2.0	(0.632, 0.367)
	0.1	10.0	1.9	(0.634, 0.365)
	1.0	10.0	1.9	(0.634, 0.365)
	3.0	10.0	1.8	(0.632, 0.368)

On the basis of well-established diagrams [49,69] and the number of Stark components arising for each Eu^{3+} transition, the symmetry site occupied by the dopants can be assigned. Deconvolution of the spectra in Fig. 3b shows splitting of the $^7F_{1,2}$ levels into three and four Stark components, respectively. Bearing in mind that we observed a $^5D_0 \rightarrow {}^7F_0$ transition, we can assume that Eu^{3+} occupies a site with lower symmetry, a subgroup of D_{2d}, the symmetry C_{2v} in this host, due to disorder promoted by the dopants introduced into the HfO_2 lattice. Liao et al. [70] came to a similar conclusion about the Eu^{3+} symmetry site in a Eu^{3+}-doped yttria stabilized zirconia (YSZ).

We also annealed Eu^{3+}-doped HfO_2 at 900 °C. Fig. 5 illustrates the emission spectra of the samples with Eu^{3+} concentration from 0.1 to 20 mol %, under excitation at 394 nm. We can clearly see the Eu^{3+} 4f intraconfigurational transitions. We followed the structural changes by observing the luminescent properties of these samples. Once again, the spectra of the samples with lower Eu^{3+} concentration (0.1 or 1.0 mol%) resemble the spectra of the monoclinic phase in Fig. 3. As for higher Eu^{3+} concentration (10.0 or 20.0 mol%), the tetragonal phase is stabilized. The samples annealed at 900 °C have similar asymmetric ratio to the samples annealed at 700 °C (Table 2), indicating that the respective phases (monoclinic or tetragonal) are formed, and that Eu^{3+} occupies the same symmetry site in the monoclinic and tetragonal phases.

This work and the literature have described that higher RE^{3+} concentration stabilizes the ZrO_2 or HfO_2 tetragonal phase. To design an efficient luminophore in the tetragonal phase, using a non-luminescent RE^{3+} constitutes an easy strategy to stabilize the desirable crystalline phase while a lower concentration of the optically active RE^{3+} is required. This prevents luminescence quenching through non-radiative energy migration between the Eu^{3+} ions due to the short distance between them in the host. The same strategy has been adopted to stabilize the ZrO_2 and HfO_2 crystalline phases by incorporation of RE^{3+}, such as Y, Gd, Lu, and La, while maintaining the luminescence of other RE^{3+}, such as Eu^{3+} and Tb^{3+}, at smaller quantity [31,32,70–76]. Therefore, to evaluate the effect of increasing Eu^{3+} concentration in the tetragonal phase only, we doped HfO_2 with a fixed concentration of 10 mol% La^{3+} and varied the Eu^{3+} concentration.

Fig. 6 depicts the emission spectra of 10 mol% La^{3+}/x mol% Eu^{3+} (*x*

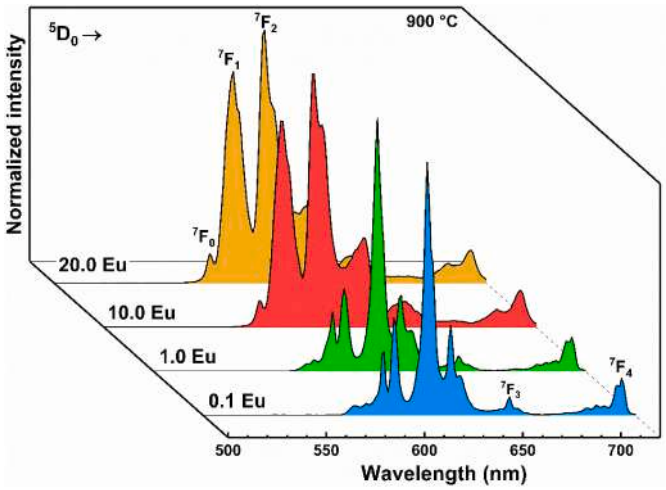

Fig. 5. Emission spectra under excitation at 394 nm of Eu^{3+}-doped HfO_2 annealed at 900 °C.

= 0.1, 1, or 3 mol%) co-doped HfO_2 under excitation at 394 nm. All the spectra present inhomogeneous broad emission bands and the characteristic spectral profile of HfO_2 in the tetragonal crystalline phase containing high Eu^{3+} concentration, proving that this specific phase is stabilized in all the co-doped samples. The minimum difference between the spectra in terms of the hypersensitive $^5D_0 \rightarrow {}^7F_2$ transition is related mostly to Eu^{3+} occupying slightly different sites in this disordered host [76]. As can be seen in Table 2, the $^5D_0 \rightarrow {}^7F_2/{}^5D_0 \rightarrow {}^7F_1$ ratios of these three co-doped HfO_2 are close to each other and to the values of Eu^{3+}-doped HfO_2, indicating that Eu^{3+} occupies the same average symmetry sites.

We estimated the emission color of these systems by calculating the (*x,y*) color coordinates (Table 2) from the emission spectra of the samples by considering only the Eu^{3+} transition (excitation at 394 nm). Fig. 7 depicts the *Commission Internationale d'Éclairage* (CIE) 1931 chromaticity diagram. For the systems where Eu^{3+} is in the monoclinic HfO_2 structure, the $^5D_0 \rightarrow {}^7F_2$ transition is intense, as seen in the corresponding spectra, resulting in redder emission. Upon increasing Eu^{3+} concentration and stabilization of the tetragonal structure, where Eu^{3+} is in a more symmetric center, the electric dipole transitions become more forbidden, and the $^5D_0 \rightarrow {}^7F_1$ transition predominates, leading to an orange-red emission. For the samples with lower Eu^{3+} concentration, but tetragonally stabilized with La^{3+}, the same orange-red emission arises.

Fig. 8 shows the $^5D_0$ excited state emission decay curves for Eu^{3+}-doped and La^{3+}/Eu^{3+} co-doped HfO_2 annealed at 900 °C, under excitation at 394 nm and fixed emission at the maximum intensity band of the $^5D_0 \rightarrow {}^7F_2$ transition (606 or 614 nm), according to the emission spectra in Figs. 6 and 7. The curves behave close to a single exponential and can thus be fitted by using a first-order exponential. Although we have discussed that Eu^{3+} occupies slightly distinct symmetry sites due to the disordered structures (Hf^{4+} and Eu^{3+} have mismatched ionic radii and oxygen vacancies), as observed from inhomogeneous broadening of the emission bands, the monoexponentially fitted curves indicate that these ions are located at sites with close lifetimes. The lifetime values from decay curves are presented in Table 3. The only exception is HfO_2 doped with 0.1 mol% Eu^{3+}, fitted with a second-order exponential, where the short lifetime with a minor contribution is probably related to non-radiative processes that can reduce the $^5D_0$ excited state lifetime. Therefore, for comparative purposes, we obtained the value presented in Table 3 for 0.1 mol% Eu^{3+}-doped HfO_2 by integrating the area of the decay curve ($\tau_{1/e}$).

The difference in symmetry sites when Eu^{3+} is embedded into the two different crystalline phases also reflects on the lifetime values. HfO_2 doped with 1 mol% Eu^{3+} has lower lifetime as compared to HfO_2 co-doped with 1 mol% Eu^{3+}/10 mol% La^{3+}. These samples have the same Eu^{3+} concentration, but the local environment of Eu^{3+} completely different. In the first case, assigned as the monoclinic phase, Eu^{3+} replaces Hf^{4+} in a lower symmetry site, so it has higher transition probability and shorter lifetime. In contrast, Eu^{3+} incorporated into the tetragonal phase, stabilized by La^{3+}, has longer lifetime, which is consistent with the higher symmetry of the site that Eu^{3+} occupies in this host, as expected by observation of the emission spectra.

For the samples with tetragonal phase stabilized with a fixed La^{3+} concentration, we evaluated the influence of the variation in Eu^{3+} concentration in this particular host lattice. Increasing the Eu^{3+} concentration from 0.1 to 3 mol% slightly lengthens the lifetime. Stabilization with a non-luminescent RE^{3+}, such as La^{3+}, allows tetragonal HfO_2 with lower Eu^{3+} concentration to be obtained. Therefore, at the same time, we achieved phase control with a small amount of Eu^{3+}, which could be homogeneously distributed in the host lattice with a sufficiently large average Eu^{3+}-Eu^{3+} distance, allowing the Eu^{3+} ions to exist as isolated luminescent centers. This prevents Eu^{3+} clusters from being formed and avoids the non-radiative losses that would diminish the lifetime values.

However, the opposite occurs at higher Eu^{3+} concentration. The tetragonal phase can also be stabilized by larger amount of Eu^{3+}. Nevertheless, the Eu^{3+}-Eu^{3+} distance shortens with increasing Eu^{3+} concentration, to culminate in luminescence quenching processes due to energy migration between Eu^{3+} ions in combination with host defects, which drastically diminishes the $^5D_0$ lifetime. Hence, HfO_2 doped with 10 and 20 mol% Eu^{3+} are representatively presented in Fig. 8 to show the reduction in lifetime: despite tetragonal phase stabilization, the luminescence efficiency decreases with high Eu^{3+} content.

We calculated the radiative transition probabilities (A_{0J}), the total radiative probability (A_T), the radiative lifetime (τ_{RAD}), the intrinsic quantum yield (Q_{Eu}^{Eu}) of the Eu^{3+} $^5D_0$ energy level [77] (Table 3), and the Judd-Ofelt (JO) parameters [78,79] (Table 4) on the basis of the emission spectra presented in Figs. 5 and 6, fitted by Lorentzian functions, under excitation at 394 nm. Usually, JO parameters of trivalent lanthanides-doped materials are calculated from their absorption spectra [49,80], from where it can be predicted the oscillator strengths, luminescence branching rations, excited state radiative lifetimes, and, thus, evaluate the intrinsic quantum yield [78,79,81]. For Eu^{3+}-doped materials, the calculation on the intensity parameters from the absorption spectra is difficult since the intensity of only a few absorptions bands has sufficient intensity in the visible range to do the calculations [82]. However, Eu^{3+} ions have unique properties that allows the JO parameters calculations from the emission spectra. As previously discussed, the magnetic dipole (MD) transition ($^5D_0 \rightarrow {}^7F_1$) has the dipole strength independent on the chemical environment [83], enabling the use of this transition as a reference.

The $^5D_0 \rightarrow {}^7F_1$ transition radiative probability (A_{01}) for a specific host is given by:

$$A_{01} = A'_{01} n^3 \quad (1)$$

where A'_{01} is the probability of this transition in vacuum ($A'_{01} = 14.65\ s^{-1}$) [82,83] and n is the refractive index of the host. Thus, the probability is given by:

$$A_{01} = 3,1 \times 10^{-12} \tilde{\nu}^3 n^3 \quad (2)$$

where $\tilde{\nu}$ is $^5D_0 \rightarrow {}^7F_1$ transition barycenter (in cm^{-1}) and $3,1 \times 10^{-12}$ is a constant for Eu^{3+} ions.

Therefore, the intensity of this transition is used as a reference for the other transitions originating from the $^5D_0$ excited state and their intensity (I_{0J}) can be expressed in terms of the integrated areas under the emission bands (S_{0J}) in their luminescence spectrum [82]:

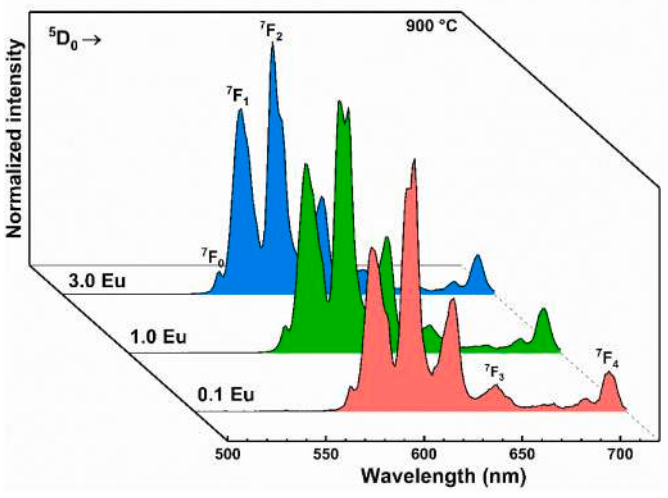

Fig. 6. Emission spectra under excitation at 394 nm of Eu^{3+}-doped HfO_2 containing 10 mol% La^{3+} and annealed at 900 °C.

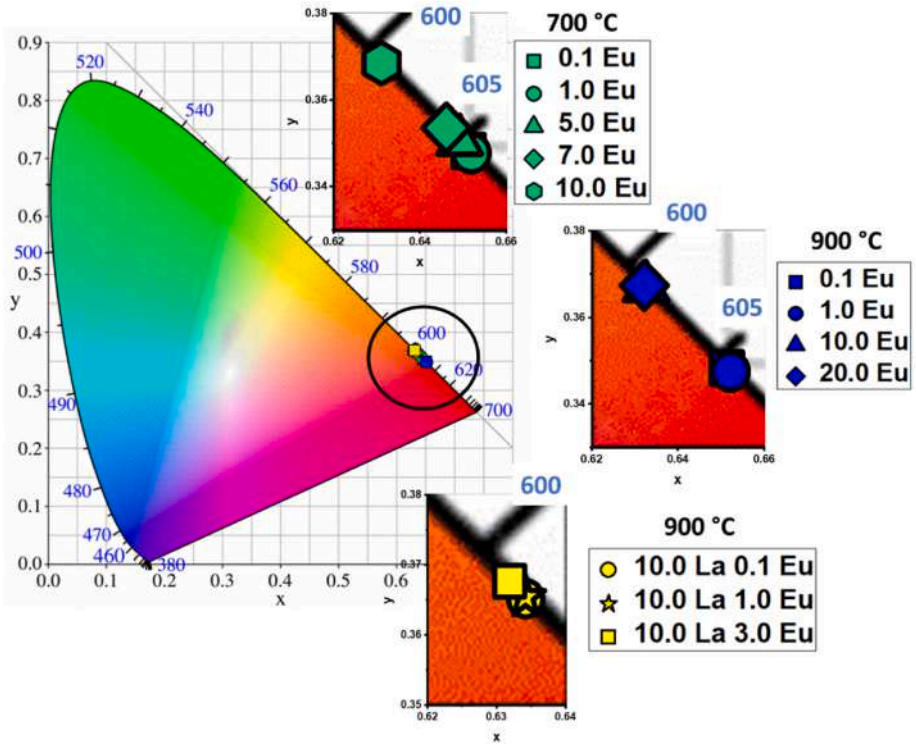

Fig. 7. CIE 1931 chromaticity diagram of Eu^{3+}-doped and La^{3+}/Eu^{3+} co-doped HfO_2 annealed at 700 and 900 °C (excitation at 394 nm).

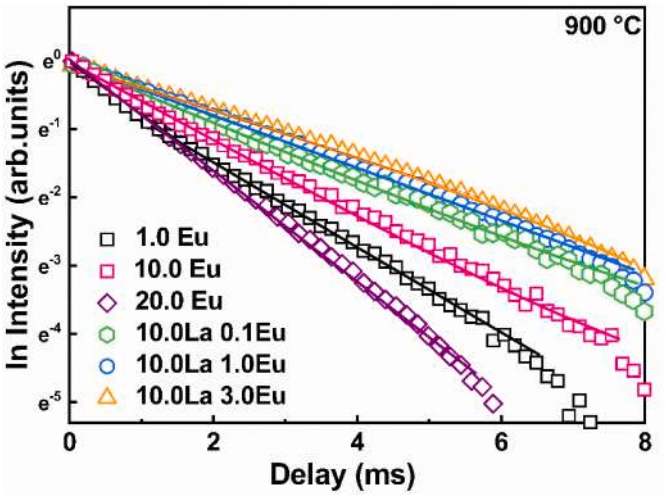

Fig. 8. Decay curves of the $^5D_0$ excited state of Eu^{3+} in HfO_2 (with and without 10 mol% La^{3+}) under excitation at 394 nm.

$$I_{0J} = hc\tilde{\nu}A_{0J}N_{(^5D_0} \equiv S_{0J} \quad (3)$$

The total radiative probability (A_T) of Eu^{3+} transitions from $^5D_0$ is given by:

$$A_T = \sum_{J=0}^{6} A_{0J} = \frac{A_{01}}{S_{01}} \times \sum_{J=0}^{6} S_{0J} \quad (4)$$

The radiative probability of $^5D_0 \rightarrow {}^7F_2$ (A_{02}) and $^5D_0 \rightarrow {}^7F_4$ (A_{04}) is calculated by Ref. [84]:

$$A_{02} = \left(\frac{S_{02}}{S_{01}}\right) A_{01} \quad (5)$$

Table 4
Judd-Ofelt parameters of the $^5D_0$ emitting level under excitation at 394 nm of Eu^{3+}-doped and Eu^{3+}/La^{3+} co-doped HfO_2 annealed at 900 °C.

Eu^{3+} concentration (mol %)	La^{3+} concentration (mol %)	Ω_2 (10^{-20} cm^2)	Ω_4 (10^{-21} cm^2)
1.0	–	5.1	16.3
10	–	3.1	8.8
20	–	3.1	8.6
0.1	10	3.0	8.7
1.0	10	2.9	8.4
3.0	10	2.7	7.6

Table 3
Intrinsic quantum yield of the $^5D_0$ emitting level of Eu^{3+}-doped and Eu^{3+}/La^{3+} co-doped HfO_2 annealed at 900 °C under excitation at 394 nm.

Eu^{3+} concentration (mol %)	La^{3+} concentration (mol %)	$A_{0\text{-}1}$ (s^{-1})	$A_{0\text{-}2}$ (s^{-1})	$A_{0\text{-}4}$ (s^{-1})	A_T (s^{-1})	τ_{RAD} (ms)	τ_{EXP} (ms) (±0.1 ms)	Q^{Eu}_{Eu} (%)
1.0	–	101	338	51	490	2.0	1.3[a]	64
10	–	103	207	28	338	3.0	1.7	57
20	–	103	206	27	336	3.0	1.2	40
0.1	10	103	197	27	327	3.1	2.3	75
1.0	10	103	195	26	324	3.1	2.6	84
3.0	10	103	182	24	308	3.2	3.1	96

[a] $\tau_{1/e}$ value.

$$A_{04} = \left(\frac{S_{04}}{S_{01}}\right) A_{01} \tag{6}$$

Therefore, A_T is given by the sum of A_{01}, A_{02}, and A_{04}:

$$A_T = \sum_{J=0}^{4} A_{0J} \tag{7}$$

$$A_T = \frac{1}{\tau_{RAD}} \tag{8}$$

The intrinsic quantum yield (Q_{Eu}^{Eu}) is determined by:

$$\left(Q_{Eu}^{Eu}\right) = \frac{\tau_{EXP}}{\tau_{RAD}} \tag{9}$$

The refractive index we used for these calculations was 1.9 for all the systems because in a previous work [18] this value was estimated by using specular reflectance of dip-coated HfO_2 films with different RE^{3+} concentration prepared by the same methodology. Irrespective of the RE^{3+} concentration, the same value of refractive index was obtained.

As expected, lower symmetry sites possess higher A_T values, which results in a relaxation of the selection rules and allows a mixture of f-d configurations [77]. In this case, Eu^{3+} embedded in the HfO_2 monoclinic phase (sample doped with 1 mol % Eu^{3+}), with lower symmetry, presents higher A_T value, and the intrinsic quantum yield is about 64%. With increasing Eu^{3+} concentration and tetragonal phase stabilization, Eu^{3+} should occupy a site with higher symmetry site, and higher radiative lifetime would be expected. Nevertheless, luminescence quenching takes place, leading to a lower experimental lifetime and reducing the Q_{Eu}^{Eu} values for 10 and 20 mol% Eu^{3+}-doped HfO_2. On the other hand, tetragonal HfO_2 stabilized with La^{3+} has increased intrinsic quantum yield—the A_T values are close, but the slight increase in the experimental lifetime values leads to higher Q_{Eu}^{Eu} values, with outstanding results of up to 96%.

The JO parameters (Ω_λ) are obtained by the following equation [82]:

$$\Omega_\lambda = \frac{3h}{64\pi^4 e^2 \nu^{-3}} \frac{9}{n(n^2+2)^2} \frac{1}{\left|\left\langle {}^5D_0 \middle\| U^{(\lambda)} \middle\| {}^7F_J \right\rangle\right|^2} A_{0J} \tag{10}$$

Table 4 displays the experimental Ω_2 and Ω_4 intensity parameter values of these samples. Ω_2 is related to the degree of covalence, and the higher Ω_2 values of the systems in the monoclinic HfO_2 phase suggests a more covalent and polarizable chemical environment for Eu^{3+}, related to the higher hypersensitivity behavior of its $^5D_0 \rightarrow {}^7F_2$ transition. The lower Ω_2 values of the tetragonal phase systems indicate that Eu^{3+} is in a less polarizable and more symmetric environment, in agreement with the asymmetric ratio presented in Table 2.

All these results indicate that the strategy adopted enables the synthesis, phase control, and luminescent property tunability of HfO_2 systems, to reach outstanding intrinsic quantum yield values without luminescence quenching. These results point out to the design of an efficient red-emitting nanometric system whose structure can be tailored for the desired application. This paves the way for important technological optical applications of these systems that are beneficial for the fields of photonics and biophotonics, including optical biomarkers, scintillators, displays, LEDs, lasers, and waveguides.

4. Conclusion

Stable colloidal suspensions containing pure and Eu^{3+}-doped HfO_2 nanoparticles in ethanolic medium were successfully prepared. The average nanoparticle size is 4–6 nm, as verified by PCS and HRTEM, and microscopy revealed formation of monoclinic HfO_2. HfO_2 nanoparticles containing 0.1 up to 20 mol% Eu^{3+} were obtained. The different doping concentrations do not influence the average nanoparticle size. XRD analysis of the Eu^{3+}-doped HfO_2 powder annealed at 700 °C indicates formation of two crystalline phases: at lower Eu^{3+} concentration (up to 5 mol%), the monoclinic phase emerges; at Eu^{3+} concentration higher than 10 mol%, the high-temperature tetragonal phase can be stabilized at lower temperature.

We followed the structural changes taking place upon increasing Eu^{3+} concentration by the emission spectra of the samples. Different spectral profiles for the different crystalline structures (monoclinic and tetragonal) were obtained. The Eu^{3+} spectra present broad emission bands, which evidence microdeformations in the host HfO_2 lattice. Such deformations promote various slightly distinct symmetry sites. On the basis of the analysis of the relative intensity of the Stark components and the asymmetry ratio, Eu^{3+} occupies higher symmetry site in the tetragonal than in the monoclinic structure, as expected.

We successfully designed rare earth ion-stabilized tetragonal HfO_2 that allowed the Eu^{3+} ions to be dispersed in the host lattice as isolated luminescent centers, thereby avoiding the luminescence quenching process. More specifically, we investigated the Eu^{3+} luminescent properties in tetragonal HfO_2 doped with a fixed concentration of 10 mol% La^{3+} and various Eu^{3+} concentrations, up to 3 mol %. The resulting systems present long lifetime and high intrinsic quantum yield values, in contrast to the lower parameters obtained for tetragonal HfO_2 stabilized with high Eu^{3+} concentration only.

In this sense, we have demonstrated an effective and facile strategy to stabilize different HfO_2 polymorphs doped with rare earth ions while tailoring their structure and tuning the emission properties. The results showed that a non-optically active ion, such as La^{3+}, provides tetragonal HfO_2 stabilization without compromising the luminescence intensity of Eu^{3+} This fact suggests homogeneous Eu^{3+} distribution in the crystalline structure, preventing cluster formation and luminescence quenching.

Funding

This work was financially supported by Brazilian funding agencies Fapesp (grant number 2017/11301-2, 2020/05319-9, 2021/08111-2, and scholarship process number 2020/00277-6), CNPq, and CAPES.

CRediT authorship contribution statement

Fernanda Hediger Borges: Investigation, Spectroscopic measurements, Data curation, Conceptualization, Validation, Writing – original draft, Writing – review & editing. **Douglas Silva da Hora Oliveira:** Investigation, Spectroscopic measurements, Data curation. **Giulia Paulino Hernandes:** Investigation, Spectroscopic measurements, Data curation. **Sidney José Lima Ribeiro:** Conceptualization, Supervision. **Rogéria Rocha Gonçalves:** Supervision, Resources, Funding acquisition, Investigation, Spectroscopic measurements, Data curation, Conceptualization, Validation, Writing – original draft, Writing – review & editing.

Declaration of competing interest

The authors declare the following financial interests/personal relationships which may be considered as potential competing interests: Rogeria Rocha Goncalves reports financial support was provided by National Council for Scientific and Technological Development. Rogeria Rocha Goncalves reports financial support was provided by State of Sao Paulo Research Foundation. Fernanda Hediger Borges reports financial support was provided by State of Sao Paulo Research Foundation. Rogeria R goncalves reports a relationship with State of Sao Paulo Research Foundation that includes: funding grants.

Data availability

Data will be made available on request.

Acknowledgments

The authors acknowledge the Brazilian funding agencies FAPESP (Fundação de Amparo à Pesquisa do Estado de São Paulo), CNPq (Conselho Nacional de Desenvolvimento Científico e Tecnológico), and CAPES (Coordenação de Aperfeiçoamento de Pessoal de Nível Superior) for financial support. This work was developed within the scope of the FAPESP project 2020/05319–9. F. H. Borges acknowledges FAPESP for the scholarship process number 2020/00277-6. R.R.G. acknowledges CNPq (grant number 303110/2019–8) and FAPESP (grant number 2020/05319-9, 2021/0811-2, and 2017/11301-2) for financial support. We also thank Mrs. Cynthia Maria de Campos Prado Manso for reviewing the text and the Department of Chemistry – FFCLRP, University of São Paulo for the opportunity of using its facilities.

References

[1] H. Fujimori, M. Yashima, S. Sasaki, M. Kakihana, T. Mori, M. Tanaka, M. Yoshimura, Internal distortion in ceria-doped hafnia solid solutions: high-resolution x-ray diffraction and Raman scattering, Phys. Rev. B Condens. Matter 64 (13) (2001) 1–5.

[2] M.M. Opeka, I.G. Talmy, J.A. Zaykoski, Oxidation-based materials selection for 2000 °C+ hypersonic aerosurfaces: theoretical considerations and historical experience, J. Mater. Sci. 39 (19) (2004) 5887–5904.

[3] C.C. Wang, S.A. Akbar, W. Chen, V.D. Patton, Electrical properties of high-temperature oxides, borides, carbides, and nitrides, J. Mater. Sci. 30 (7) (1995) 1627–1641.

[4] K. Mergia, V. Liedtke, T. Speliotis, G. Apostolopoulos, S. Messoloras, Thermo-mechanical behaviour of HfO_2 coatings for aerospace applications, Adv. Mater. Res. 59 (2009) 87–91.

[5] E.N. Kablov, V.L. Stolyarova, V.A. Vorozhtcov, S.I. Lopatin, S.M. Shugurov, A. L. Shilov, F.N. Karachevtsev, P.N. Medvedev, Vaporization and thermodynamics of ceramics in the Sm_2O_3-Y_2O_3-HfO_2 system, Rapid Commun. Mass Spectrom. 34 (8) (2020).

[6] C.K. Roy, M. Noor-A-Alam, A.R. Choudhuri, C.V. Ramana, Synthesis and microstructure of Gd_2O_3-doped HfO_2 ceramics, Ceram. Int. 38 (3) (2012) 1801–1806.

[7] C. Li, Y. Ma, Z. Xue, Y. Yang, J. Chen, H. Guo, Effect of Y doping on microstructure and thermophysical properties of yttria stabilized hafnia ceramics, Ceram. Int. 44 (15) (2018) 18213–18221.

[8] J. Wang, H.P. Li, R. Stevens, Hafnia and hafnia-toughened ceramics, J. Mater. Sci. 27 (20) (1992) 5397–5430.

[9] X. Zhao, D. Vanderbilt, First-principles study of structural, vibrational, and lattice dielectric properties of hafnium oxide, Phys. Rev. B 65 (233106) (2002).

[10] J.H. Choi, Y. Mao, J.P. Chang, Development of hafnium based high-k materials - a review, Mater. Sci. Eng. R Rep. 72 (6) (2011) 97–136.

[11] T.S. Böscke, J. Müller, D. Bräuhaus, U. Schröder, U. Böttger, Ferroelectricity in hafnium oxide thin films, Appl. Phys. Lett. 99 (10) (2011).

[12] M.H. Park, D.H. Lee, K. Yang, J.-Y. Park, G.T. Yu, H.W. Park, M. Materano, T. Mittmann, P.D. Lomenzo, T. Mikolajick, U. Schroeder, C.S. Hwang, Review of defect chemistry in fluorite-structure ferroelectrics for future electronic devices, J. Mater. Chem. C 8 (31) (2020) 10526–10550.

[13] F. Ali, D. Zhou, M. Ali, H.W. Ali, M. Daaim, S. Khan, M.M. Hussain, N. Sun, Recent progress on energy-related applications of HfO_2 -based ferroelectric and antiferroelectric materials, ACS Appl. Electron. Mater. 2 (8) (2020) 2301–2317, https://doi.org/10.1021/acsaelm.0c00304.

[14] J.P. Lehan, Y. Mao, B.G. Bovard, H.A. Macleod, Optical and microstructural properties of hafnium dioxide thin films, Thin Solid Films 203 (2) (1991) 227–250.

[15] T. Nishide, S. Honda, M. Matsuura, M. Ide, Surface, structural and optical properties of sol-gel derived HfO_2 films, Thin Solid Films 371 (1) (2000) 61–65.

[16] M.C. Cheynet, S. Pokrant, F.D. Tichelaar, J.L. Rouvìre, Crystal structure and band gap determination of HfO_2 thin films, J. Appl. Phys. 101 (5) (2007), 054101.

[17] M.A. Krebs, R.A. Condrate, Vibrational spectra of HfO_2-ZrO_2 solid solutions, J. Am. Ceram. Soc. 65 (9) (1982) c144–c145.

[18] C.D.S. Cunha, J.L. Ferrari, S.J.L. Ribeiro, M. Ferrari, R.R. Gonçalves, Tailoring the structure and luminescence of nanostructured Er^{3+} and Er^{3+}/Yb^{3+}-activated hafnia-based systems, J. Am. Ceram. Soc. 98 (10) (2015) 3136–3144.

[19] M. Alvisi, M. Di Giulio, S.G. Marrone, M.R. Perrone, M.L. Protopapa, A. Valentini, L. Vasanelli, HfO_2 films with high laser damage threshold, Thin Solid Films 358 (1) (2000) 250–258.

[20] G. Abromavičius, S. Kičas, R. Buzelis, High temperature annealing effects on spectral, microstructural and laser damage resistance properties of sputtered HfO_2 and HfO_2-SiO_2 mixture-based UV mirrors, Opt. Mater. 95 (2019), 109245.

[21] R.R. Gonçalves, Y. Messaddeq, A. Chiasera, Y. Jestin, M. Ferrari, S.J.L. Ribeiro, Erbium-activated silica-zirconia planar waveguides prepared by sol-gel route, Thin Solid Films 516 (10) (2008) 3094–3097.

[22] R.R. Gonçalves, G. Carturan, M. Montagna, M. Ferrari, L. Zampedri, S. Pelli, G. C. Righini, S.J.L. Ribeiro, Y. Messaddeq, Erbium-activated HfO_2-based waveguides for photonics, Opt. Mater. 25 (2) (2004) 131–139. Elsevier.

[23] R.R. Gonçalves, G. Carturan, L. Zampedri, M. Ferrari, A. Chiasera, M. Montagna, G. C. Righini, S. Pelli, S.J.L. Ribeiro, Y. Messaddeq, Infrared-to-visible CW frequency upconversion in erbium activated silica-hafnia waveguides prepared by sol-gel route, J. Non-Cryst. Solids 322 (1–3) (2003) 306–310.

[24] L. Zampedri, G.C. Righini, H. Portales, S. Pelli, G.N. Conti, M. Montagna, M. Mattarelli, R.R. Gonçalves, M. Ferrari, A. Chiasera, M. Bouazaoui, C. Armellini, Sol - gel-derived Er-activated SiO_2-HfO_2 planar waveguides for 1.5 μm application, J. Non-Cryst. Solids 345–346 (2004) 580–584.

[25] R.R. Gonçalves, G. Carturan, L. Zampedri, M. Ferrari, M. Montagna, A. Chiasera, G. C. Righini, S. Pelli, S.J.L. Ribeiro, Y. Messaddeq, Sol-gel Er-doped SiO_2-HfO_2 planar waveguides: a viable system for 1.5 μm application, Appl. Phys. Lett. 81 (1) (2002) 28–30.

[26] C.E. Curtis, L.M. Doney, J.R. Johnson, Some properties of hafnium oxide, hafnium silicate, calcium hafnate, and hafnium carbide, J. Am. Ceram. Soc. 37 (10) (1954) 458–465.

[27] C.T. Lynch, 6 - Hafnium oxide, in: A.M. Alper (Ed.), High Temperature Oxides 5, Elsevier, 1970, pp. 193–216.

[28] J. Meng, D. Jiang, Q. Li, Luminescent properties of Eu^{3+}-doped HfO_2 powders prepared by combustion, Key Eng. Mater. 434–435 (3) (2010) 805–807.

[29] A. Wiatrowska, E. Zych, Modeling luminescent properties of HfO_2:Eu powders with Li, Ta, Nb, and v codopants, J. Phys. Chem. C 116 (10) (2012) 6409–6419.

[30] M. Molina Higgins, A. Banu, S. Pendleton, J.V. Rojas, Radiocatalytic performance of oxide-based nanoparticles for targeted therapy and water remediation, Radiat. Phys. Chem. 173 (2020).

[31] A. Lauria, I. Villa, M. Fasoli, M. Niederberger, A. Vedda, Multifunctional role of rare earth doping in optical materials: nonaqueous sol-gel synthesis of stabilized cubic HfO_2 luminescent nanoparticles, ACS Nano 7 (8) (2013) 7041–7052.

[32] M. Villanueva-Ibañez, C. Le Luyer, C. Dujardin, J. Mugnier, Elaboration, structural and spectroscopic properties of rare earth-doped yttrium-hafnium sol-gel oxide powders for scintillation applications, Mater. Sci. Eng. B: Solid State Mater. Adv. Technol. 105 (1–3) (2003) 12–15. Elsevier.

[33] A. Wiatrowska, E. Zych, L. Kpiński, Monoclinic HfO_2:Eu X-ray phosphor, Radiat. Meas. 45 (3–6) (2010) 493–496. Pergamon.

[34] L.R.H. Gerken, K. Keevend, Y. Zhang, F.H.L. Starsich, C. Eberhardt, G. Panzarasa, M.T. Matter, A. Wichser, A. Boss, A. Neels, I.K. Herrmann, Lanthanide-doped hafnia nanoparticles for multimodal theranostics: tailoring the physicochemical properties and interactions with biological entities, ACS Appl. Mater. Interfaces 11 (1) (2019) 437–448.

[35] A.D. Furasova, A.F. Fakhardo, V.A. Milichko, E. Tervoort, M. Niederberger, V. V. Vinogradov, Synthesis of a rare-earth doped hafnia hydrosol: towards injectable luminescent nanocolloids, Colloids Surf. B Biointerfaces 154 (2017) 21–26.

[36] V. Jayaraman, G. Bhavesh, S. Chinnathambi, S. Ganesan, P. Aruna, Synthesis and characterization of hafnium oxide nanoparticles for bio-safety, Mater. Express 4 (5) (2014) 375–383.

[37] L. Maggiorella, G. Barouch, C. Devaux, A. Pottier, E. Deutsch, J. Bourhis, E. Borghi, L. Levy, Nanoscale radiotherapy with hafnium oxide nanoparticles, Future Oncol. 8 (9) (2012) 1167–1181.

[38] I. Villa, C. Villa, A. Monguzzi, V. Babin, E. Tervoort, M. Nikl, M. Niederberger, Y. Torrente, A. Vedda, A. Lauria, Demonstration of cellular imaging by using luminescent and anti-cytotoxic europium-doped hafnia nanocrystals, Nanoscale 10 (17) (2018) 7933–7940.

[39] J. Kaszewski, J. Olszewski, J. Rosowska, B. Witkowski, Ł. Wachnicki, K. Wenelska, E. Mijowska, Z. Gajewski, M. Godlewski, M.M. Godlewski, HfO_2:Eu nanoparticles excited by X-rays and UV-visible radiation used in biological imaging, J. Rare Earths 37 (11) (2019) 1176–1182.

[40] R.D. Shannon, Revised effective ionic radii and systematic studies of interatomic distances in halides and chalcogenides, Acta Crystallogr. A 32 (5) (1976) 751–767.

[41] Z.D. Dohcevic-Mitrovic, N. Paunović, B. Matović, P. Osiceanu, R. Scurtu, S. Aškrabić, M. Radović, Structural dependent room-temperature ferromagnetism in yttrium doped HfO_2 nanoparticles, Ceram. Int. 41 (5) (2015) 6970–6977.

[42] D. Fischer, A. Kersch, Stabilization of the high-tetragonal phase in : the influence of dopants and temperature from ab initio simulations, J. Appl. Phys. 104 (2008), 84104.

[43] B. Cojocaru, D. Avram, R. Negrea, C. Ghica, V.G. Kessler, G.A. Seisenbaeva, V. I. Parvulescu, C. Tiseanu, Phase control in Hafnia: new synthesis approach and convergence of average and local structure properties, ACS Omega 4 (5) (2019) 8881–8891.

[44] C.-K. Lee, E. Cho, H.-S. Lee, C.S. Hwang, S. Han, First-principles study on doping and phase stability of HfO_2, Phys. Rev. B 78 (1) (2008) 1–4.

[45] C. Dubourdieu, E. Rauwel, H. Roussel, F. Ducroquet, B. Holländer, M. Rossell, G. Van Tendeloo, S. Lhostis, S. Rushworth, Addition of yttrium into HfO_2 films: microstructure and electrical properties, J. Vac. Sci. Technol. A Vacuum, Surfaces, Film. 27 (3) (2009) 503–514.

[46] E.R. Andrievskaya, Phase equilibria in the refractory oxide systems of zirconia, hafnia and yttria with rare-earth oxides, J. Eur. Ceram. Soc. 28 (12) (2008) 2363–2388.

[47] P. Li, I.-W. Chen, J.E. Penner-Hahn, Effect of dopants on zirconia stabilization—an X-ray absorption study: II, tetravalent dopants, J. Am. Ceram. Soc. 77 (5) (1994) 1281–1288.

[48] Y.K. Voron'ko, M.A. Zufarov, A.A. Sobol, S.N. Ushakov, L.I. Tsymbal, Spectroscopy and structure of Eu^{3+} centers in partially stabilized zirconia and hafnia, Inorg. Mater. 33 (4) (1997).

[49] K. Binnemans, Interpretation of europium(III) spectra, Coord. Chem. Rev. 295 (2015) 1–45.

[50] F.H. Borges, F.J. Caixeta, R.R. Pereira, S. Ruella de Oliveira, R.A.S. Ferreira, R. R. Gonçalves, High Eu^{3+} concentration quenching in Y_3TaO_7 solid solution for orange-reddish emission in photonics, RSC Adv. 10 (29) (2020) 16917–16927.

[51] S. Kumar, S.B. Rai, C. Rath, Latent fingerprint imaging using Dy and Sm codoped HfO_2 nanophosphors: structure and luminescence properties, Part. Part. Syst. Charact. 36 (6) (2019) 1–11.

[52] K. Momma, F. Izumi, VESTA 3 for three-dimensional visualization of crystal, volumetric and morphology data, J. Appl. Crystallogr. 44 (6) (2011) 1272–1276.

[53] R.E. Hann, P.R. Suitch, J.L. Pentecost, Monoclinic crystal structures of ZrO_2 and HfO_2 refined from X-ray powder diffraction data, J. Am. Ceram. Soc. 68 (10) (1985) C-285–C-286.

[54] R. Ruh, P.W.R. Corfield, Crystal structure of monoclinic hafnia and comparison with monoclinic zirconia, J. Am. Ceram. Soc. 53 (3) (1970) 126–129.

[55] R. Wu, B. Zhou, Q. Li, Z. Jiang, W. Wang, W. Ma, X. Zhang, Elastic and vibrational properties of monoclinic HfO_2 from first-principles study, J. Phys. D Appl. Phys. 45 (2012) 8.

[56] G. Teufer, The crystal structure of tetragonal ZrO_2, Acta Crystallogr. 15 (11) (1962), 1187–1187.

[57] B. Matović, D. Bučevac, M. Prekajski, V. Maksimović, D. Gautam, K. Yoshida, T. Yano, Synthesis and characterization of nanometric yttrium-doped hafnia solid solutions, J. Eur. Ceram. Soc. 32 (9) (2012) 1971–1976.

[58] V.V. Popov, A.P. Menushenkov, A.A. Yastrebtsev, A.A. Pisarev, I.V. Shchetinin, M. V. Zheleznyi, Y.V. Zubavichus, L.A. Arzhatkina, N.A. Tsarenko, Influence of the concentration and lanthanoide type on the phase transitions in Ln_2O_3-MO_2 system (Ln = La, Gd, Y; M = Zr, Hf), J. Phys. Conf. Ser. 941 (1) (2018).

[59] V. Sánchez Escribano, E. Fernández López, M. Panizza, C. Resini, J.M. Gallardo Amores, G. Busca, Characterization of cubic ceria-zirconia powders by X-ray diffraction and vibrational and electronic spectroscopy, Solid State Sci. 5 (10) (2003) 1369–1376.

[60] V. Milman, A. Perlov, K. Refson, S.J. Clark, J. Gavartin, B. Winkler, Structural, electronic and vibrational properties of tetragonal zirconia under pressure: a density functional theory study, J. Phys. Condens. Matter 21 (48) (2009).

[61] J. Guzmán Mendoza, E. Garfias García, J.C. Guzmán Olguín, E. Montes, G. Torres Jasso, M. García-Hipólito, C. Falcony-Guajardo, Changes induced in the luminescent emission of Eu^{3+} by different crystal nature: an analysis by group theory, J. Lumin. 188 (April) (2017) 394–399.

[62] S. Lange, V. Kiisk, V. Reedo, M. Kirm, J. Aarik, I. Sildos, Luminescence of RE-ions in HfO_2 thin films and some possible applications, Opt. Mater. 28 (11) (2006) 1238–1242.

[63] S. Stojadinović, N. Tadić, A. Ćirić, R. Vasilić, Photoluminescence properties of Eu^{3+} doped HfO_2 coatings formed by plasma electrolytic oxidation of hafnium, Opt. Mater. 77 (2018) 19–24.

[64] J. Dexpert-Ghys, M. Faucher, P. Caro, Site selective spectroscopy and structural analysis of yttria-doped zirconias, J. Solid State Chem. 54 (2) (1984) 179–192.

[65] E. Fernandez Lopez, V. Sanchez Escribano, M. Panizza, M.M. Carnasciali, G. Busca, Vibrational and electronic spectroscopic properties of zirconia powders, J. Mater. Chem. 11 (7) (2001) 1891–1897.

[66] S.F. Wang, F. Gu, M.K. Lü, Z. Sen Yang, G.J. Zhou, H.P. Zhang, Y.Y. Zhou, S. M. Wang, Structure evolution and photoluminescence properties of ZrO_2:Eu^{3+} nanocrystals, Opt. Mater. 28 (10) (2006) 1222–1226.

[67] R. Reisfeld, E. Zigansky, M. Gaft, Europium probe for estimation of site symmetry in glass films, glasses and crystals, Mol. Phys. 102 (11-12 SPEC. ISS.) (2004) 1319–1330.

[68] L.K. Dash, N. Vast, P. Baranek, M.-C. Cheynet, L. Reining, Electronic structure and electron energy-loss spectroscopy of ZrO_2 zirconia, Phys. Rev. B 70 (24) (2004), 245116.

[69] P.A. Tanner, Lanthanide Luminescence in Solids, Springer, Berlin, Heidelberg, 2010, pp. 183–233.

[70] J. Liao, D. Zhou, B. Yang, R. Liu, Q. Zhang, Sol-gel preparation and photoluminescence properties of tetragonal ZrO_2:Y^{3+}, Eu^{3+} nanophosphors, Opt. Mater. 35 (2) (2012) 274–279.

[71] E.A. Agarkova, M.A. Borik, T.V. Volkova, A.V. Kulebyakin, I.E. Kuritsyna, E. E. Lomonova, F.O. Milovich, V.A. Myzina, P.A. Ryabochkina, N.Y. Tabachkova, Ionic conductivity, phase composition, and local defect structure of ZrO_2-Gd_2O_3 system solid solution crystals, J. Solid State Electrochem. 23 (9) (2019) 2619–2626.

[72] Y. Hui, Y. Zhao, S. Zhao, L. Gu, X. Fan, L. Zhu, B. Zou, Y. Wang, X. Cao, Fluorescence of Eu^{3+} as a probe of phase transformation of zirconia, J. Alloys Compd. 573 (2013) 177–181.

[73] L. Liang, H. Zhou, G. Wu, Z. Mo, D. Bao, Dielectric properties and bright red emission of Y^{3+}/Eu^{3+}-codoped ZrO_2 thin films prepared by chemical solution deposition, Ceram. Int. 39 (2) (2013) 1335–1340.

[74] C. LeLuyer, M. Villanueva-Ibañez, A. Pillonnet, C. Dujardin, HfO_2:X (X = Eu^{3+}, Ce^{3+}, Y^{3+}) sol gel powders for ultradense scintillating materials, J. Phys. Chem. A 112 (41) (2008) 10152–10155.

[75] E. Zych, M. Wójtowicz, A. Dobrowolska, L. Kepiński, Radioluminescence and photoluminescence of hafnia-based Eu-doped phosphors, Opt. Mater. 31 (12) (2009) 1764–1767.

[76] M. Eibl, S. Shaw, D. Prieur, A. Rossberg, M.C. Wilding, C. Hennig, K. Morris, J. Rothe, T. Stumpf, N. Huittinen, Understanding the local structure of Eu^{3+}- and Y^{3+}-stabilized zirconia: insights from luminescence and X-ray absorption spectroscopic investigations, J. Mater. Sci. 55 (23) (2020) 10095–10120.

[77] F.J. Caixeta, F.T. Aquino, R.R. Pereira, R.R. Gonçalves, Highly red luminescent Nb_2O_5:Eu^{3+} nanoparticles in silicate host for solid-state lighting and energy conversion, Opt. Mater. 111 (2021), 110671.

[78] B.R. Judd, Optical absorption intensities of rare-earth ions, Phys. Rev. 127 (3) (1962) 750–761.

[79] G.S. Ofelt, Intensities of crystal spectra of rare-earth ions, J. Chem. Phys. 37 (3) (1962) 511–520.

[80] M.P. Hehlen, M.G. Brik, K.W. Krämer, 50th anniversary of the Judd-Ofelt theory: an experimentalist's view of the formalism and its application, J. Lumin. 136 (2013) 221–239.

[81] A. Ćirić, S. Stojadinović, M. Sekulić, M.D. Dramićanin, JOES: an application software for Judd-Ofelt analysis from Eu^{3+} emission spectra, J. Lumin. 205 (2019) 351–356.

[82] L.D. Carlos, R.A.S. Ferreira, V. De Zea Bermudez, S.J.L. Ribeiro, Lanthanide-containing light-emitting organic–inorganic hybrids: a bet on the future, Adv. Mater. 21 (5) (2009) 509–534.

[83] M.H.V. Werts, R.T.F. Jukes, J.W. Verhoeven, The emission spectrum and the radiative lifetime of Eu^{3+} in luminescent lanthanide complexes, Phys. Chem. Chem. Phys. 4 (9) (2002) 1542–1548.

[84] I.P. Assunção, A.N. Carneiro Neto, R.T. Moura, C.C.S. Pedroso, I.G.N. Silva, M.C.F. C. Felinto, E.E.S. Teotonio, O.L. Malta, H.F. Brito, Odd-even effect on luminescence properties of europium aliphatic dicarboxylate complexes, ChemPhysChem 20 (15) (2019) 1931–1940.